

## PAPER

[View Article Online](#)  
[View Journal](#) | [View Issue](#)Cite this: *J. Mater. Chem. A*, 2023, **11**, 4013Manipulating selective amine transformation pathways via cocatalyst-modified monolayer ZnIn<sub>2</sub>S<sub>4</sub> photocatalysts†Jian-Hui Zheng, Ming-Yu Qi, Zi-Rong Tang \* and Yi-Jun Xu \*

Semiconductor-based artificial photoredox-catalyzed organic synthesis offers a promising and green opportunity to harness solar energy for green organic chemistry. However, the precise manipulation of product selectivity over semiconductor-based photocatalysts for selective organic synthesis remains challenging. In this work, we report the rational preparation and application of two kinds of cocatalyst, (RuS<sub>2</sub> or Cu<sub>2</sub>S)-decorated monolayer ZnIn<sub>2</sub>S<sub>4</sub>, for the selective dehydrocoupling of aromatic amines into tunable C=N coupled imines or C–N coupled secondary amines, respectively, under visible light irradiation. The presence of the RuS<sub>2</sub> or Cu<sub>2</sub>S cocatalyst not only facilitates the charge carrier separation and migration owing to the well-matched energy band structure, but also maneuvers the interfacial charge transfer routes for the selectivity switching between C=N and C–N product formation. This work would inspire the rational design of ingenious semiconductor-based composites toward selective modulation in heterogeneous photocatalytic organic synthesis.

Received 1st January 2023  
Accepted 18th January 2023

DOI: 10.1039/d3ta00001j

[rsc.li/materials-a](https://rsc.li/materials-a)

## Introduction

Solar energy-driven organic synthesis over semiconductor-based photocatalysts offers an appealing and sustainable alternative for commodities and fine chemical synthesis, due to the fact that such a paradigm bypasses the traditional industrial routes that involve the use of toxic reagents and complex operational procedures, thus featuring eco-friendly green organic synthesis.<sup>1–3</sup> Amines, one of the most versatile structural motifs, have been characterized to synthesize a series of value-added N-containing compounds, such as imines, diamines, secondary amines, and imidazoles, by direct photochemical C–C/C–N coupling of amines.<sup>4–6</sup> In particular, in contrast to extraneous functional groups and oxidizing agents required in conventional strategies, such a photochemical C–C/C–N coupling of amines is directly triggered by the highly reactive amine radicals generated through the proton–electron transfers between amine molecules and the light-driven semiconductor-based photocatalysts (TiO<sub>2</sub>, BiVO<sub>4</sub>, CdS, *etc.*) under ambient conditions.<sup>7–9</sup> Despite these impressive research advances, a straightforward and functional strategy is to synthesize the structurally diverse N-containing compounds starting from the same set of readily accessible amines, which has rarely been implemented. Hence, the realization of a highly

selective divergent synthesis of coupling products in heterogeneous photocatalytic amine coupling synthesis requires the rational design of photocatalysts with the ability to switch the selectivity by various reaction pathways.

Within an extensive variety of metallic chalcogenides, 2D semiconductor ZnIn<sub>2</sub>S<sub>4</sub> (ZIS), especially those with atomically thick layers, have recently been identified as promising materials for building efficient, green, and sustainable artificial photosystems.<sup>10–14</sup> Thanks to their high specific surface areas, excellent charge carrier separation rate, and abundant surface sites, ZIS semiconductors offer novel and versatile possibilities to utilize sunlight for amine conversion reactions.<sup>15–18</sup> For instance, Li's group reported the application of a Pd single-atom modified ZIS composite for coupled efficient H<sub>2</sub> production and highly selective oxidation of benzylamine to *N*-benzylbenzaldimine.<sup>19</sup> Lei and co-workers synthesized the type II heterostructure ZnIn<sub>2</sub>S<sub>4</sub>@ZnO to realize highly selective photocatalytic amine reforming for the production of imines with H<sub>2</sub>.<sup>20</sup> However, these strategies target the point of efficient formation of single imine products, rather than the divergent synthesis of coupling products over ZIS composite semiconductor photocatalysts. The rational construction of cocatalyst-decorated composite photocatalysts with matchable band levels can not only facilitate charge separation, but also shift the actual oxidation/reduction catalytic sites by regulating the charge transfer path, providing a promising way for manipulating the selectivity toward the divergent synthesis of amines.<sup>21</sup>

In this work, we report a convenient approach to the divergent synthesis of amine-coupled N-containing compounds by

College of Chemistry, State Key Laboratory of Photocatalysis on Energy and Environment, Fuzhou University, Fuzhou, 350116, China. E-mail: zrtang@fzu.edu.cn; yjxu@fzu.edu.cn

† Electronic supplementary information (ESI) available: Experimental details, 19 figures and 2 tables. See DOI: <https://doi.org/10.1039/d3ta00001j>

decorating RuS<sub>2</sub> or Cu<sub>2</sub>S on monolayer ZIS (MS<sub>x</sub>/ZIS, M = Ru, Cu). Compared with the blank ZIS, the constructed composites demonstrate a significantly enhanced conversion of aromatic amines. Loading RuS<sub>2</sub> or Cu<sub>2</sub>S onto ZIS effectively enhances the ability of light absorption and photo-generated electron–hole separation of ZIS, which is attributed to the compact interfacial contact and the adaptation of the energy band structure. Moreover, the formation of band levels controls the charge transfer pathway and therefore alters the catalytic site of the reduction half-reaction. The selective tuning of C–N *versus* C=N products is successfully achieved based on the difference of reduction ability of semiconductors. Our strategy could open new horizons for the construction of function-oriented composite photocatalysts for other target applications of switching the selectivity of photocatalytic organic transformations.

## Results and discussion

Fig. 1a depicts a schematic diagram of the synthesis of ZIS and *in situ* deposition of metal sulfide cocatalysts. Scanning electron microscopy (SEM) can preliminarily confirm that the bulk ZIS is effectively exfoliated (Fig. S1†). After standing for a long time, the exfoliated ZIS can still be stably dispersed in water solvent, which is a remarkable feature of thin-layer materials.<sup>22</sup> Atomic force microscopy (AFM) further confirms the formation of exfoliated ZIS. The thickness of ZIS is approximately 1.5 nm, which is close to the thickness of a monolayer ZIS (Fig. S2†).<sup>12</sup> The clearer morphology observation and lattice analysis of ZIS are performed by high-resolution transmission electron microscopy (HRTEM). As shown in Fig. S3,† ZIS exhibits an ultrathin and transparent 2D sheet structure, and the lattice

fringe of 0.324 nm is attributed to the (102) crystal plane of ZIS.<sup>23</sup> Electron microscopy images show that the cocatalyst modified ZIS still maintains the original lamellar structure (Fig. S4†), which is supposed to be the result of the subsequent modification. In addition to the lattice fringes corresponding to ZIS, the interplanar spacing of 0.274 nm in the Cu<sub>2</sub>S/ZIS composite sample can also be clearly defined in Fig. 1b and can be considered as the (200) crystal plane of Cu<sub>2</sub>S (JCPDS no. 84-1770).<sup>24,25</sup> However, HRTEM of RuS<sub>2</sub>/ZIS can only observe the lattice fringes of hexagonal ZIS (Fig. 1c and S5†). Considering that the formation of crystalline RuS<sub>2</sub> usually requires a high-temperature annealing process, the RuS<sub>2</sub> on ZIS presented here ought to be amorphous.<sup>26,27</sup> Additionally, energy dispersive spectroscopy (EDS)-mapping also shows trace amounts of Cu or Ru (Fig. 1d and f). As shown by the X-ray diffraction (XRD) results (Fig. S6†), the lattice of ZIS does not change significantly after metal sulfide deposition, suggesting no obvious loaded particles in the composite samples. The HRTEM and EDS results of the composite samples together indicate the high distribution and dispersion of MS<sub>x</sub> (M = Ru, Cu) on the surface.<sup>28</sup>

The surface chemical valence states of the composite samples are further analyzed by X-ray photoelectron spectroscopy (XPS). The elements of relevance can all be detected in the wide-scan survey spectrum (Fig. S7†). As shown in Fig. 2a–c, the binding energies of Zn 2p at 1022.02 eV (2p<sub>3/2</sub>) and 1045.04 eV (2p<sub>1/2</sub>), In 3d at 445.04 eV (3d<sub>5/2</sub>) and 452.57 eV (3d<sub>3/2</sub>), and S 2p

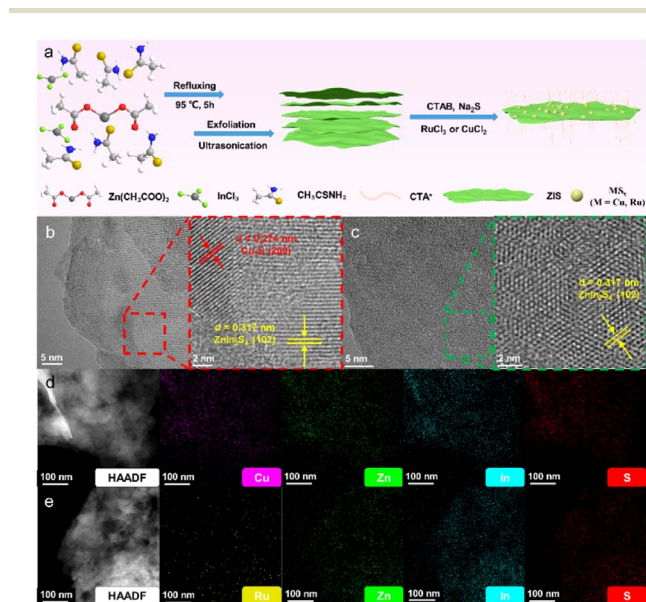


Fig. 1 (a) Schematic illustration of the fabrication of ZIS and MS<sub>x</sub>/ZIS. HRTEM images of (b) Cu<sub>2</sub>S/ZIS and (c) RuS<sub>2</sub>/ZIS. High-angle annular dark field and corresponding elemental maps of (d) Cu<sub>2</sub>S/ZIS and (e) RuS<sub>2</sub>/ZIS.

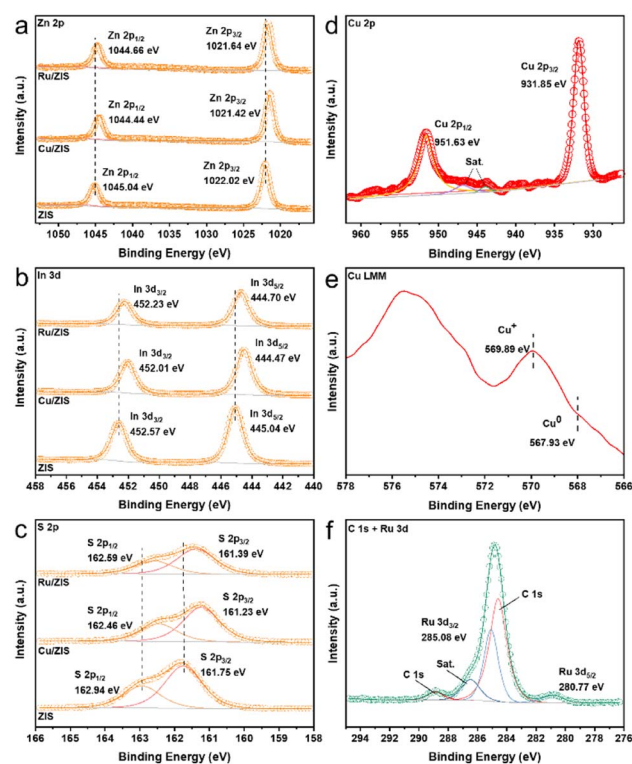
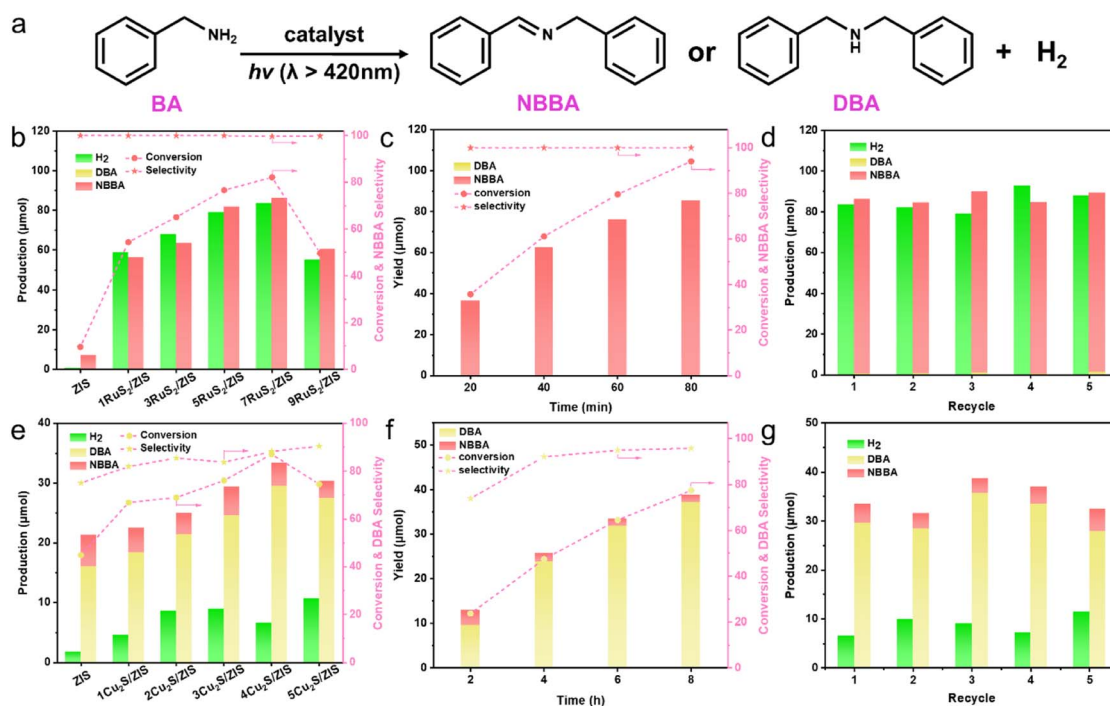


Fig. 2 XPS spectra of (a) Zn 2p, (b) In 3d, and (c) S 2p of ZIS, Cu<sub>2</sub>S/ZIS and RuS<sub>2</sub>/ZIS. (d) Cu 2p and (e) Cu LMM XPS spectra of Cu<sub>2</sub>S/ZIS. (f) C 1s and Ru 3d XPS spectra of RuS<sub>2</sub>/ZIS.

at 161.75 eV ( $2p_{3/2}$ ) and 162.94 eV ( $2p_{1/2}$ ) can be assigned to  $Zn^{2+}$ ,  $In^{3+}$  and  $S^{2-}$  of ZIS, respectively.<sup>18,29,30</sup> In addition, it can be seen that the binding energies of ZIS characteristic peaks move to a slightly lower value after the introduction of metal elements Cu and Ru, indicating the strong electronic interaction between  $MS_x$  ( $M = Ru, Cu$ ) and ZIS.<sup>31</sup> The loading of  $Cu_2S$  leads to a larger shift in the XPS characteristic peaks of ZIS, which may be attributed to the formation of a particularly strong internal electric field between the semiconductors.<sup>25,32</sup> The existence states of Cu and Ru are further analyzed. The binding energies of Cu  $2p_{3/2}$  and Cu  $2p_{1/2}$  are 931.85 and 951.63 eV (Fig. 2d), which are attributed to the peak positions of  $Cu^+/Cu^0$ . Combined with the position of the binding energy of 569.89 eV ( $Cu^+$ ) in the Auger spectrum (Fig. 2e), the valence state of Cu can be finally judged to be +1.<sup>33</sup> There is no obvious characteristic peak near the binding energy of 567.93 eV, indicating that  $Cu^0$  is not present.<sup>34</sup> The binding energies of Ru  $3d_{5/2}$  and Ru  $3d_{3/2}$  are 280.77 and 285.08 eV (Fig. 2f), which are close to the value for Ru in the +4 valence state.<sup>35,36</sup> Therefore, the supported metal sulfides on ZIS can be identified as  $Cu_2S$  and  $RuS_2$ .

With benzylamine (BA) as a model substrate, BA is controllably converted to *N*-benzylbenzaldimine (NBBA) or dibenzylamine (DBA) in  $CH_3CN$  solution containing 0.2 mmol of BA and 5 mg of sample ( $RuS_2/ZIS$  or  $Cu_2S/ZIS$ ) irradiated with a xenon lamp ( $\lambda > 420$  nm) under ambient conditions (Fig. 3a and S8†). As displayed in Fig. 3b and e, with the extension of the reaction time from 1 h to 6 h, the primary product of the BA coupling reaction over ZIS switches from

NBBA to DBA, which may be due to the hydrogenation reduction reaction of NBBA catalyzed by ZIS. The optimal  $7RuS_2/ZIS$  exhibits significantly enhanced NBBA and  $H_2$  production compared with ZIS; meanwhile, the BA conversion improves from 9.6% to 82% (Fig. 3b). The molar ratio of the oxidation product (NBBA) to the reduction product ( $H_2$ ) is close to 1 : 1, indicating a stoichiometric dehydrogenation coupling reaction.<sup>37</sup> Furthermore, the optimal apparent quantum yield (AQY) of  $H_2$  over  $7RuS_2/ZIS$  reaches 2.93% at  $\lambda = 430$  nm (Fig. S9†). Conversely, the optimal  $4Cu_2S/ZIS$  requires 6 h of irradiation to achieve a BA conversion efficiency of 87% (Fig. 3e), and the main product of DBA can be obtained with a selectivity of 88%. The selective generation of DBA can be explained by the speculation that BA is first converted to NBBA on blank ZIS and  $Cu_2S/ZIS$ , and then the hydrogenation reaction occurs to form DBA, which is also responsible for the decrease in the yield of  $H_2$ . The time-dependent analysis for NBBA production over  $7RuS_2/ZIS$  is shown in Fig. 3c and S10a,† where the amount of NBBA increases with the duration of light exposure and a high selectivity (>99%) is maintained throughout the process. As for  $4Cu_2S/ZIS$ , the selectivity of DBA gradually improves with the increase of reaction time, and reaches 96% at 8 h (Fig. 3f and S10b†). Afterwards, the recycle stability of the catalyst for the reaction was evaluated. After five replicate experiments, there is no obvious decrease in the yield of NBBA/DBA over either  $7RuS_2/ZIS$  or  $4Cu_2S/ZIS$  (Fig. 3d and g), suggesting that  $7RuS_2/ZIS$  and  $4Cu_2S/ZIS$  possess the favorable photostability.



**Fig. 3** (a) Formula for the photoredox reaction coupling BA oxidation and  $H_2$  evolution. (b) Photocatalytic performance over bare ZIS and  $RuS_2/ZIS$  with different contents of  $RuS_2$ , and the reaction time is 1 h. (c) Long-term photoactivity tests over  $7RuS_2/ZIS$ . (d) Recycle tests of  $7RuS_2/ZIS$ . (e) Photocatalytic performance over bare ZIS and  $Cu_2S/ZIS$  with different contents of  $Cu_2S$ , and the reaction time is 6 h. (f) Long-term photoactivity tests over  $4Cu_2S/ZIS$ . (g) Recycle tests of  $4Cu_2S/ZIS$ .



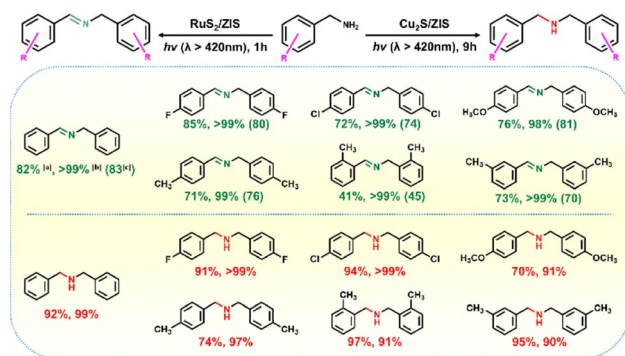


Fig. 4 Photocatalytic conversion of various aromatic amines. Reaction conditions: 0.2 mmol of BA, 10 mL of CH<sub>3</sub>CN, 10 mg of catalyst, Ar atmosphere, 300 W xenon lamp. <sup>a</sup>Conversion (%). <sup>b</sup>Selectivity (%). <sup>c</sup>Yield of H<sub>2</sub> (μmol).

Aiming to assess the generality of the photocatalytic conversion of various aromatic amines to C=N or C–N products by RuS<sub>2</sub>/ZIS and Cu<sub>2</sub>S/ZIS, the photocatalytic performance of aromatic amines with different substituents has been investigated (Fig. 4 and S11–S16<sup>†</sup>). The selectivity of the C=N products over RuS<sub>2</sub>/ZIS always approaches 100%. The conversion efficiency of different aromatic amines is not at the same level, which should be caused by the disparity of substituent groups and the spatial site resistance. The influence of the substitution group is consistent with that reported in earlier work.<sup>38,39</sup> Moreover, the yield of H<sub>2</sub> obtained in the different substituent reactions is associated with the amine conversion, which indicates that these reactions are also stoichiometric. During the substrate broadening experiments with Cu<sub>2</sub>S/ZIS, the reaction time is extended to 9 h to obtain a relatively higher aromatic amine conversion. The various C–N products are also obtained with outstanding selectivity of above 90%. The formation of secondary amines consumes H<sup>+</sup> and thus the H<sub>2</sub> evolution completely ceases.

A series of electrochemical and photochemical characterization studies have been performed to investigate the reasons for the enhanced activity of MS<sub>x</sub>/ZIS composites. The linear sweep voltammetry (LSV) curves (Fig. 5a) show that the composites significantly enhance the current density compared to the blank ZIS, and the improvement is more pronounced for RuS<sub>2</sub>/ZIS. These results indicate that the introduction of cocatalysts promotes charge transfer and reduces the H<sub>2</sub> evolution overpotential.<sup>23</sup> Cyclic voltammetry (CV) curves (Fig. 5b) depict similar results, illustrating that electrons move more efficiently in the interfacial area between the electrode and the electrolyte agent.<sup>29</sup> In addition, MS<sub>x</sub>/ZIS composites show a smaller arc radius in the Nyquist plot at high frequency in electrochemical impedance spectroscopy (EIS). RuS<sub>2</sub>/ZIS has the smallest semicircle (Fig. 5c), indicating lower resistance between the composite and electrolyte and better charge transfer.<sup>30</sup> The steady-state PL characterization further validates the above results (Fig. S17<sup>†</sup>). The PL strength of Cu<sub>2</sub>S/ZIS is higher than that of RuS<sub>2</sub>/ZIS, and the strength of ZIS is the highest, suggesting that the construction of MS<sub>x</sub>/ZIS composites

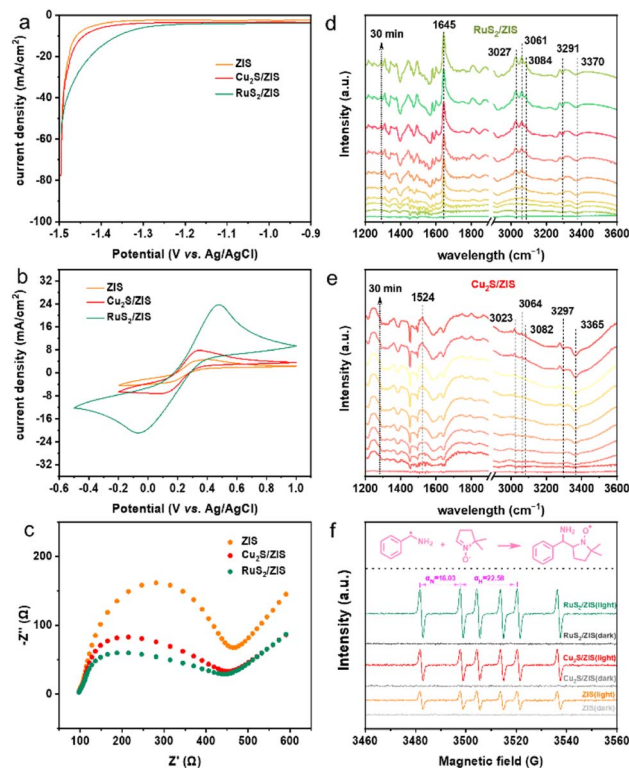


Fig. 5 (a) Polarization curves, (b) CV curves and (c) EIS Nyquist plots of ZIS, Cu<sub>2</sub>S/ZIS and RuS<sub>2</sub>/ZIS. *In situ* FTIR spectra of (d) RuS<sub>2</sub>/ZIS and (e) Cu<sub>2</sub>S/ZIS. (f) EPR spectra of ZIS, Cu<sub>2</sub>S/ZIS and RuS<sub>2</sub>/ZIS in BA solution with or without visible light irradiation.

effectively suppresses the recombination of photoexcited electron–hole pairs. In addition, the optical absorption properties of the samples are tested by using ultraviolet–visible diffuse reflectance spectra (DRS) (Fig. S18a<sup>†</sup>). The absorption threshold of ZIS is about 560 nm, which shows strong visible light absorption. There is a marked change in the light absorption intensity of the composite samples, suggesting that the loading of cocatalysts promotes the light absorption ability of ZIS. In particular, for RuS<sub>2</sub>/ZIS, the absorption in the visible light range is significantly improved. The band gap energy of ZIS is calculated to be 2.36 eV according to the Tauc diagram (Fig. S18b<sup>†</sup>). Based on the results of Mott–Schottky curves (Fig. S18c<sup>†</sup>), the conduction band and valence band of ZIS can be calculated to be approximately −1.20 V and 1.16 V (vs. NHE), respectively (Fig. S18d<sup>†</sup>).

To further investigate the photocatalytic reaction mechanism of aromatic amines over MS<sub>x</sub>/ZIS (M = Ru, Cu), a series of control and quenching experiments with BA as the reaction substrate are first carried out (Tables S1 and S2<sup>†</sup>). The blank photocatalytic reaction is unworkable without the presence of a catalyst or light, which demonstrates that the reaction is actuated by photocatalysis. When electron scavenger carbon tetrachloride (CCl<sub>4</sub>) is added to the reaction system, all reduction reactions requiring electrons are greatly inhibited. The decrease in the rate of H<sub>2</sub> evolution also leads to a decrease in the rate of RuS<sub>2</sub>/ZIS-catalyzed BA conversion (entry 4, Table

S1†), illustrating that the oxidation and reduction reactions in this system are critically interrelated.<sup>40</sup> Significantly, upon adding  $\text{CCl}_4$ , the main product in the  $\text{Cu}_2\text{S}/\text{ZIS}$  catalyst system changes from DBA to NBBA (entry 4, Table S2†), which indicates that the formation of DBA is subjected to the reductive hydrogenation of NBBA, and this process is probably the rate-limiting step of the whole procedure. The introduction of hole scavenger triethanolamine (TEOA) directly suppresses the conversion of BA, which proves that the oxidation half-reaction of BA is driven by holes. With the entry of radical trapping agent 5,5-dimethyl-1-pyrroline *N*-oxide (DMPO) into the reaction system, the photoactivity is simultaneously inhibited, denoting the formation of radical intermediates during the reaction. TEOA and DMPO also hinder the formation of DBA, probably because the trapping agents interfere with the adsorption and activation of the reaction intermediates over the catalyst surface.

The variations of the reactants and products over  $\text{MS}_x/\text{ZIS}$  are further investigated by *in situ* Fourier transformed infrared (FTIR) spectroscopy (Fig. 5d and e). The peaks at  $3291\text{ cm}^{-1}$  and  $3370\text{ cm}^{-1}$  in the spectra of  $\text{RuS}_2/\text{ZIS}$ , and at  $3297\text{ cm}^{-1}$  and  $3365\text{ cm}^{-1}$  on the spectra of  $\text{Cu}_2\text{S}/\text{ZIS}$  with reduced intensity can be assigned to the symmetrical stretching vibration ( $V_s$ ) and asymmetrical stretching vibration ( $V_{as}$ ) of the N–H bond, respectively.<sup>41</sup> The peaks at  $3027\text{ cm}^{-1}$ ,  $3061\text{ cm}^{-1}$  and  $3084\text{ cm}^{-1}$  in the spectrum of  $\text{RuS}_2/\text{ZIS}$ , and the characteristic peaks at  $3023\text{ cm}^{-1}$ ,  $3064\text{ cm}^{-1}$  and  $3082\text{ cm}^{-1}$  in the spectrum of  $\text{Cu}_2\text{S}/\text{ZIS}$ , are assigned to the stretching vibration of the C–H bond in the benzene ring.<sup>41,42</sup> The new band formed at  $1643\text{ cm}^{-1}$  in Fig. 5d corresponds to the CN dual bond,<sup>43</sup> indicating the generation of imines. In contrast, a novel band emerges at  $1524\text{ cm}^{-1}$  in Fig. 5e, which can be attributed to the bending vibration of the N–H bond for the secondary amine.

With the purpose of obtaining the radical intermediate mechanism, the electron paramagnetic resonance (EPR) technique is employed to detect the radical intermediate formed during the catalytic process using DMPO as the spin trap. The measurement results are shown in Fig. 5f. The radical signal could not be detected in the dark. After 10 min of irradiation, six characteristic signal peaks of similar intensity appeared in all three samples. The nitrogen hyperfine splitting ( $\alpha_N$ ) and hydrogen hyperfine splitting ( $\alpha_H$ ) are calculated to be 16.03 and 22.58, respectively, suggesting the generation of the  $\alpha$ -amino-benzyl ( $\text{Ph}(\cdot\text{CH})\text{NH}_2$ ) radical.<sup>49</sup> It is worth mentioning that the intensity order of the characteristic peaks under light ( $\text{RuS}_2/\text{ZIS} > \text{Cu}_2\text{S}/\text{ZIS} > \text{ZIS}$ ) is in accordance with the reaction activity pattern as well as the electrochemical characterization results.

In view of all of the above analysis, a potential photocatalytic mechanism for the steerable synthesis of C=N or C–N products over  $\text{RuS}_2/\text{ZIS}$  or  $\text{Cu}_2\text{S}/\text{ZIS}$  is shown in Fig. 6. Under the irradiation of visible light, the semiconductor component of the composite catalyst is excited to generate photogenerated carriers. The ultrathin properties of the monolayer ZIS are beneficial for the more efficient migration of electron–hole pairs.<sup>10</sup> The supported cocatalysts ( $\text{MS}_x$ ) can effectively capture the holes in ZIS, which not only promotes charge separation, but also prevents ZIS from photocorrosion to a certain extent.<sup>21,32,36</sup> The BA adsorbed on the catalyst surface is oxidized

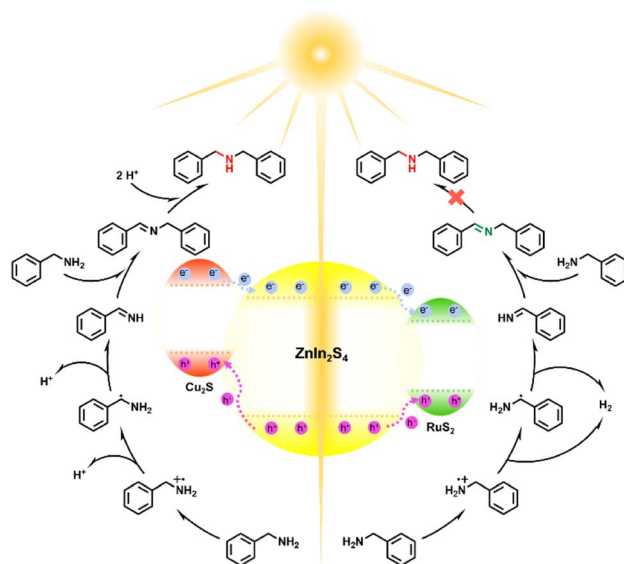


Fig. 6 Mechanism of conversion of BA to DBA or NBBA catalyzed  $\text{MS}_x/\text{ZIS}$  ( $M = \text{Cu}, \text{Ru}$ ) composites under visible light irradiation.

to *N*-benzylideneamine ( $\text{PhCH=NH}$ ) by the holes through a radical reaction process, and the nucleophilic  $\text{PhCH=NH}$  undergoes a condensation reaction with another BA to form an imine (NBBA).<sup>4,38</sup> In the presence of high-work function metal Ru, electrons will be inclined to move to  $\text{RuS}_2$  and the adsorbed  $\text{H}^+$  on Ru will be rapidly reduced to release  $\text{H}_2$ ,<sup>36</sup> thereby accelerating the formation of NBBA over  $\text{RuS}_2/\text{ZIS}$ . In contrast, being a p-type semiconductor,  $\text{Cu}_2\text{S}$  typically forms a strong electron transfer hub with an n-type ZIS semiconductor by means of a p–n junction (Fig. S19†).<sup>24,32</sup> The photoexcited electrons in this composite will tend to flow into and accumulate in the n-type ZIS semiconductor, over which the weak reductive reforming ability and the strong adsorption capacity of  $\text{S}^{2-}$  for  $\text{H}^+$  endow ZIS with the unique hydrogenation ability,<sup>44–46</sup> which therefore contributes to the further hydrogenation of the imine to a secondary amine (DBA) over the  $\text{Cu}_2\text{S}/\text{ZIS}$  catalyst.

## Conclusions

As a summary, we have demonstrated the monolayer ZIS modified with metal sulfide cocatalysts to construct  $\text{MS}_x/\text{ZIS}$  composites for aromatic amine dehydrocoupling reactions with selective switching between C=N and C–N products. The binary composite photocatalysts possess a superior conversion capacity of BA under visible light irradiation to that of blank ZIS, and exhibit enhanced charge separation efficiency and amine compatibility. The stoichiometric dehydrogenation reaction on  $\text{RuS}_2/\text{ZIS}$  exhibits high selectivity (>99%) for efficient photoredox-catalyzed  $\text{H}_2$  evolution and dehydrogenation of BA coupled to imines. Comparatively,  $\text{Cu}_2\text{S}/\text{ZIS}$  promotes the hydrogenation reduction of NBBA to DBA. The discrepancy of charge transfer pathways between metal sulfides and ZIS, together with their  $\text{H}_2$  evolution ability contributes to the product variation of BA coupling. In addition, controlled

experiments and mechanistic research together demonstrate the  $\text{Ph}(\cdot\text{CH})\text{NH}_2$  radical to be the key reaction intermediate. The present work is anticipated to provide an effective approach to address the problem of difficult selectivity tuning in semiconductor-based photocatalytic organic synthesis of fine chemicals.

## Experimental section

### Materials

All chemicals were of analytical grade and used without further purification. Zinc acetate dihydrate ( $\text{Zn}(\text{CH}_3\text{COO})_2 \cdot 2\text{H}_2\text{O}$ ), indium chloride ( $\text{InCl}_3$ ), thioacetamide ( $\text{C}_2\text{H}_5\text{NS}$ , TAA), sodium sulfide nonahydrate ( $\text{Na}_2\text{S} \cdot 9\text{H}_2\text{O}$ ), 5,5-dimethyl-1-pyrroline *N*-oxide ( $\text{C}_6\text{H}_{11}\text{NO}$ , DMPO), ruthenium trichloride ( $\text{RuCl}_3 \cdot 3\text{H}_2\text{O}$ ) and cupric chloride ( $\text{CuCl}_2$ ) were obtained from Aladdin Biochemical Technology Co., Ltd. (Shanghai, China). *N,N*-Dimethylformamide ( $\text{C}_3\text{H}_7\text{NO}$ , DMF), carbon tetrachloride ( $\text{CCl}_4$ ), acetonitrile ( $\text{CH}_3\text{CN}$ ), triethanolamine (TEOA) and absolute ethanol ( $\text{C}_2\text{H}_5\text{OH}$ ) were supplied by Sinopharm chemical reagent Co., Ltd. (Shanghai, China). Cetyltrimethylammonium bromide (CTAB) was purchased from Sigma-Aldrich. Deionized (DI) water was obtained from local sources.

### Synthesis of monolayer $\text{ZnIn}_2\text{S}_4$

The synthesis of monolayer ZIS was carried out according to the method from related literature with slight modification.<sup>10</sup> In detail, 2 mmol of  $\text{Zn}(\text{CH}_3\text{COO})_2 \cdot 2\text{H}_2\text{O}$  and 4 mmol of  $\text{InCl}_3$  were dissolved in 250 mL of DI water. After stirring for 0.5 h, 12 mmol of TAA was added and stirred for another 0.5 h. The above solution was stirred and refluxed for 5 h at 95 °C in an oil bath with a water condensing device. Subsequently, the obtained bulk ZIS was washed by centrifugation at 6000 rpm. The collected precipitate was re-dispersed with 200 mL of DI water, and the preliminary suspension was obtained by ultrasonic peeling for 2 h in an ultrasonic machine with a power of 180 W. Finally, the suspension was centrifuged at the same 6000 rpm for 10 min, and the supernatant was collected in blue cap bottles to obtain the final ZIS dispersion.

### Synthesis of metal sulfides/ $\text{ZnIn}_2\text{S}_4$ composites

The *in situ* deposition of metal sulfides on ZIS was carried out at room temperature. First, 50 mg of CTAB was dissolved in 30 mL of  $\text{C}_2\text{H}_5\text{OH}$ , and 10 mL of ZIS dispersion was slowly added dropwise, and stirred for 30 min to reach the adsorption equilibrium of CTAB on the catalyst surface. Then, 0.8 mL of  $\text{Na}_2\text{S}$  aqueous solution (0.5 M) was added and stirred for 10 min. Aqueous  $\text{RuCl}_3$  (0.01 M) was then added dropwise to the above solution. After stirring at room temperature for 30 min, the precipitate was washed with  $\text{C}_2\text{H}_5\text{OH}$  by centrifugation and suction filtration, and redispersed in 5 mL of DI water. Finally, it was freeze-dried for 12 h to obtain a solid catalyst. The composite sample is labeled as  $x\text{RuS}_2/\text{ZIS}$ , where  $x$  represents  $x \times 100 \mu\text{L}$  of  $\text{RuCl}_3$  aqueous solution added. The synthesis

method of  $x\text{Cu}_2\text{S}/\text{ZIS}$  is similar to that of  $x\text{RuS}_2/\text{ZIS}$ , except that the added metal solution is  $\text{CuCl}_2$  aqueous solution (1 mM).

### Photocatalytic performance testing

The photocatalytic selective conversion of aromatic amines was carried out in a double-glass reactor with condensed water passing through. Typically, 5 mg of catalyst was ultrasonically dispersed in 10 mL of  $\text{CH}_3\text{CN}$  containing 0.2 mmol of aromatic amine. Ar gas was bubbled for 15 min to remove air from the reactor and solvent. The reactor was then placed 10 cm in front of a 300 W xenon lamp (PLS-SXE 300D, Beijing Perfectlight Co., Ltd.) and irradiated with visible light ( $\lambda > 420 \text{ nm}$ ). The light intensity here was  $420 \text{ mW cm}^{-2}$  as measured using a PL-MW2000 photoradiometer (Beijing Perfectlight Co., Ltd.). The generated  $\text{H}_2$  was measured by gas chromatography (Shimadzu GC-2014C, 5A column, Ar carrier). The coupling products of aromatic amines were characterized and quantified by gas chromatography-mass spectrometry (Shimadzu GC-MS QP 2020, Q-Exactive).

## Author contributions

Jian-Hui Zheng: investigation, validation, writing-original draft, formal analysis, and writing-review & editing. Ming-Yu Qi: writing-review & editing and formal analysis. Zi-Rong Tang: funding acquisition, formal analysis, supervision, writing-review & editing, and resources. Yi-Jun Xu: funding acquisition, conceptualization, resources, project administration, writing-review & editing, and supervision.

## Conflicts of interest

There are no conflicts to declare.

## Acknowledgements

This work was supported by the National Natural Science Foundation of China (22072023, 22172030, 21872029, U1463204, and 21173045), the Program for National Science and Technology Innovation Leading Talents (00387072), the Program for Leading Talents of Fujian Universities, the First Program of Fujian Province for Top Creative Young Talents, and the Natural Science Foundation of Fujian Province (2019J01631 and 2017J07002).

## References

- 1 M.-Y. Qi, M. Conte, M. Anpo, Z.-R. Tang and Y.-J. Xu, *Chem. Rev.*, 2021, **121**, 13051–13085.
- 2 Y. Markushyna, P. Lamagni, J. Catalano, N. Lock, G. Zhang, M. Antonietti and A. Savateev, *ACS Catal.*, 2020, **10**, 7336–7342.
- 3 Y.-H. Li, F. Zhang, Y. Chen, J.-Y. Li and Y.-J. Xu, *Green Chem.*, 2020, **22**, 163–169.
- 4 X. Liu, D. Dai, Z. Cui, Q. Zhang, X. Gong, Z. Wang, Y. Liu, Z. Zheng, H. Cheng, Y. Dai, B. Huang and P. Wang, *ACS Catal.*, 2022, **12**, 12386–12397.

- 5 P. Wang, S. Fan, X. Li, J. Wang, Z. Liu, C. Bai, M. O. Tadé and S. Liu, *Nano Energy*, 2021, **89**, 106349.
- 6 M. Wang, L. Li, J. Lu, N. Luo, X. Zhang and F. Wang, *Green Chem.*, 2017, **19**, 5172–5177.
- 7 T. Wang, X. Tao, X. Li, K. Zhang, S. Liu and B. Li, *Small*, 2021, **17**, 2006255.
- 8 M. Lv, F. Tong, Z. Wang, Y. Liu, P. Wang, H. Cheng, Y. Dai, Z. Zheng and B. Huang, *J. Mater. Chem. A*, 2022, **10**, 19699–19709.
- 9 Y. Huang, C. Liu, M. Li, H. Li, Y. Li, R. Su and B. Zhang, *ACS Catal.*, 2020, **10**, 3904–3910.
- 10 M.-Q. Yang, Y.-J. Xu, W. Lu, K. Zeng, H. Zhu, Q.-H. Xu and G. W. Ho, *Nat. Commun.*, 2017, **8**, 14224.
- 11 R. Pan, M. Hu, J. Liu, D. Li, X. Wan, H. Wang, Y. Li, X. Zhang, X. Wang, J. Jiang and J. Zhang, *Nano Lett.*, 2021, **21**, 6228–6236.
- 12 C. Du, Q. Zhang, Z. Lin, B. Yan, C. Xia and G. Yang, *Appl. Catal., B*, 2019, **248**, 193–201.
- 13 X. Jiao, Z. Chen, X. Li, Y. Sun, S. Gao, W. Yan, C. Wang, Q. Zhang, Y. Lin, Y. Luo and Y. Xie, *J. Am. Chem. Soc.*, 2017, **139**, 7586–7594.
- 14 Y. Zhou, Z. Wang, L. Huang, S. Zaman, K. Lei, T. Yue, Z. a. Li, B. You and B. Y. Xia, *Adv. Energy Mater.*, 2021, **11**, 2003159.
- 15 L. Cheng, Q. Xiang, Y. Liao and H. Zhang, *Energy Environ. Sci.*, 2018, **11**, 1362–1391.
- 16 K. Zhang and L. Guo, *Catal. Sci. Technol.*, 2013, **3**, 1672–1690.
- 17 S. Chandrasekaran, L. Yao, L. Deng, C. Bowen, Y. Zhang, S. Chen, Z. Lin, F. Peng and P. Zhang, *Chem. Soc. Rev.*, 2019, **48**, 4178–4280.
- 18 C. Han, Y.-H. Li, J.-Y. Li, M.-Y. Qi, Z.-R. Tang and Y.-J. Xu, *Angew. Chem., Int. Ed.*, 2021, **60**, 7962–7970.
- 19 P. Wang, S. Fan, X. Li, J. Wang, Z. Liu, Z. Niu, M. O. Tadé and S. Liu, *Nano Energy*, 2022, **95**, 107045.
- 20 X. Lei, X. Yin, S. Meng, Li, H. Wang, H. Xi, J. Yang, X. Xu, Z. Yang and Z. Lei, *Mol. Catal.*, 2022, **519**, 112120.
- 21 J. Yang, D. Wang, H. Han and C. Li, *Acc. Chem. Res.*, 2013, **46**, 1900–1909.
- 22 L. Pan, Y.-T. Liu, X.-M. Xie and X.-Y. Ye, *Small*, 2016, **12**, 6703–6713.
- 23 Y.-H. Li, M.-Y. Qi, Z.-R. Tang and Y.-J. Xu, *J. Phys. Chem. C*, 2022, **126**, 1872–1880.
- 24 Y. Chen, Z. Qin, X. Wang, X. Guo and L. Guo, *RSC Adv.*, 2015, **5**, 18159–18166.
- 25 C.-C. Wang, J.-W. Chang and S.-Y. Lu, *Catal. Sci. Technol.*, 2017, **7**, 1305–1314.
- 26 Y. Xu, C. Du, Q. Shen, J. Huang, X. Zhang and J. Chen, *Chem. Eng. J.*, 2021, **417**, 129318.
- 27 Y. Xia, W. Wu, H. Wang, S. Rao, F. Zhang and G. Zou, *Nanotechnology*, 2020, **31**, 145401.
- 28 Q. Lin, Y.-H. Li, M.-Y. Qi, J.-Y. Li, Z.-R. Tang, M. Anpo, Y. M. A. Yamada and Y.-J. Xu, *Appl. Catal., B*, 2020, **271**, 118946.
- 29 C.-L. Tan, M.-Y. Qi, Z.-R. Tang and Y.-J. Xu, *Appl. Catal., B*, 2021, **298**, 120541.
- 30 J.-Y. Li, M.-Y. Qi and Y.-J. Xu, *Chin. J. Catal.*, 2022, **43**, 1084–1091.
- 31 Z. Lian, P. Xu, W. Wang, D. Zhang, S. Xiao, X. Li and G. Li, *ACS Appl. Mater. Interfaces*, 2015, **7**, 4533–4540.
- 32 X. Li, K. Dai, C. Pan and J. Zhang, *ACS Appl. Nano Mater.*, 2020, **3**, 11517–11526.
- 33 J.-Y. Kim, D. Hong, J.-C. Lee, H. G. Kim, S. Lee, S. Shin, B. Kim, H. Lee, M. Kim, J. Oh, G.-D. Lee, D.-H. Nam and Y.-C. Joo, *Nat. Commun.*, 2021, **12**, 3765.
- 34 Z. Sun, C. Yi, Z. Hameiri and S. P. Bremner, *Appl. Surf. Sci.*, 2021, **555**, 149727.
- 35 D. J. Morgan, *Surf. Interface Anal.*, 2015, **47**, 1072–1079.
- 36 A. P. Gaikwad, D. Tyagi, C. A. Betty and R. Sasikala, *Appl. Catal., A*, 2016, **517**, 91–99.
- 37 M.-Y. Qi, Y.-H. Li, M. Anpo, Z.-R. Tang and Y.-J. Xu, *ACS Catal.*, 2020, **10**, 14327–14335.
- 38 M.-Y. Qi, M. Conte, Z.-R. Tang and Y.-J. Xu, *ACS Nano*, 2022, **16**, 17444–17453.
- 39 F.-K. Shang, M.-Y. Qi, C.-L. Tan, Z.-R. Tang and Y.-J. Xu, *ACS Phys. Chem. Au*, 2022, **2**, 216–224.
- 40 G. Han, X. Liu, Z. Cao and Y. Sun, *ACS Catal.*, 2020, **10**, 9346–9355.
- 41 H. Chen, C. Liu, W. Guo, Z. Wang, Y. Shi, Y. Yu and L. Wu, *Catal. Sci. Technol.*, 2022, **12**, 1812–1823.
- 42 C. Liu, Y. Liu, Y. Shi, Z. Wang, W. Guo, J. Bi and L. Wu, *J. Colloid Interface Sci.*, 2023, **631**, 154–163.
- 43 R. H. Alzard, L. A. Siddig, A. S. Abdelhamid and A. Alzamly, *ACS Omega*, 2022, **7**, 36689–36696.
- 44 Y. Zhu, L. Wang, Y. Liu, L. Shao and X. Xia, *Appl. Catal., B*, 2019, **241**, 483–490.
- 45 D. Zhou, X. Xue, X. Wang, Q. Luan, A. Li, L. Zhang, B. Li, W. Dong, G. Wang and C. Hou, *Appl. Catal., B*, 2022, **310**, 121337.
- 46 L. Yuan, Y.-H. Li, Z.-R. Tang, J. Gong and Y.-J. Xu, *J. Catal.*, 2020, **390**, 244–250.